AIP | Physics of Plasmas

A computational investigation of the impact of aberrated Gaussian laser pulses on electron beam properties in laser-wakefield acceleration experiments

P. Cummings and A. G. R. Thomas

Citation: Phys. Plasmas **18**, 053110 (2011); doi: 10.1063/1.3587111
View online: http://dx.doi.org/10.1063/1.3587111
View Table of Contents: http://pop.aip.org/resource/1/PHPAEN/v18/i5
Published by the AIP Publishing LLC.

A computational investigation of the impact of aberrated Gaussian laser pulses on electron beam properties in laser-wakefield acceleration experiments

P. Cummings[a] and A. G. R. Thomas
Centre for Ultrafast Optical Science, The University of Michigan, Ann Arbor, Michigan 48105 USA

(Received 16 February 2011; accepted 10 April 2011; published online 31 May 2011)

Critical to the performance of any future accelerator based on the laser wakefield accelerator is the response of the system to perturbations from ideal. In this paper, we use particle-in-cell simulation using a modified version of the OSIRIS 2.0 framework to demonstrate that comatic optical aberrations in a nominally Gaussian laser pulse are self-corrected by the plasma response, leading to stable propagation and therefore little variation in peak energy, energy spread, or peak current of the accelerated bunch, even for serious aberrations. However, the comatic aberration does lead to enhanced transverse beam emittance in the direction of the coma. Although this may be deleterious to the performance of an accelerator, one useful outcome is that the increased oscillation amplitude of electrons in the wake structure may lead to increased synchrotron radiation emission, which would be partially polarized in the direction of coma. © *2011 American Institute of Physics*. [doi:10.1063/1.3587111]

I. INTRODUCTION

Laser wakefield acceleration[1] (LWFA) is a promising technique for generating high-energy electron beams via the interaction of a femtosecond-scale laser pulse with a plasma. The laser pulse drives a highly nonlinear plasma wake field in which electrons are trapped and accelerated well beyond the wake group velocity, $v_g \approx c$. This technique boasts acceleration gradients of $\sim$100 GeV/m (Ref. 2) or more, roughly 3 orders of magnitude greater than conventional RF technology. As a result, LWFA may ultimately enable "bench-top"-scale particle accelerators capable of producing beam energies in the GeV range over distances on the order of $\sim$1 cm or less, eliminating the large facilities currently required by RF synchrotron technology.

Synchrotrons are powerful tools because of their ability to produce controlled, focused, high-brightness light beams. Synchrotron radiation has a wide array of diverse technological and scientific applications, including cancer therapy,[3] materials characterization,[4] and nanoscale imaging.[5] However, current synchrotron technology is based on radio frequency (RF) cavities with accelerating gradients on the order of $\sim$100 MeV/m,[6] requiring facility sizes on the order of $\sim$100m (Ref. 7) or more to produce beams of the necessary energy levels. These facility sizes severely limit the availability of synchrotron technology.

The LWFA scheme has shown particular promise in terms of generating synchrotron radiation as the electron bunch tends to naturally oscillate within the plasma bubble, resulting in an effect similar to a wiggler.[8] LWFA devices can produce spatially coherent radiation pulses that are on the ultrashort (i.e., femtosecond) timescale, with a brightness in excess of 10^{22} photons per second per mrad^2 per mm^2 per 0.1% bandwidth.[9] The source produces hard x-rays, with $1-100$ keV photon energies.[9]

Realizing practical devices based on the LWFA scheme will require an understanding of the sensitivity of the system's performance as an accelerator to deviations from the ideal physics of the LWFA regime. Parameters of interest for characterizing the system's performance include the peak beam energy, beam emittance,[10] and peak beam current. One major possible deviation of the system from the idealized physics consists of deviations from Gaussian in the pulse intensity profile. Additional deviations from an ideal pulse can take the form of aberrations in the phase front and variations in the temporal profile of the pulse, which can modify the laser pulse propagation.[11–13]

Furthermore, recent experimental results[14] indicate that the introduction of a comatic aberration in a LWFA system can enhance the production of synchrotron x-rays via an increase in the betatron oscillation amplitude. An analysis of the response of the LWFA system will enable supporting this research by providing robust computational tools for introducing a comatic aberration to a LWFA system and analyzing the system's response to that aberration.

Computational methods provide an ideal avenue of investigation for these problems, as both the shape and magnitude of the pulse shape's deviation from the Gaussian can be precisely controlled. In particular, the particle-in-cell (PIC) method is an ideal computational method for studying the highly kinetic, collisionless, relativistic plasmas found in LWFA systems. This paper therefore presents the results of a computational investigation into the impact of non-Gaussian pulse intensity profiles, stemming from the comatic optical aberration, on the performance of a LWFA-based electron accelerator.

[a]Electronic mail: cummingp@umich.edu, cummi13d@gmail.com.

II. BACKGROUND

A. Overview of the diffraction theory of optical aberrations

Here we briefly review the diffraction theory of optics. In this theory, optical aberrations are characterized by an expansion of a diffraction integral[15]

$$U(u,v,\psi) = -\frac{i}{\lambda}\frac{Aa^2}{R^2}e^{i\left(\frac{R}{a}\right)^2 u} \times \int_0^1\int_0^{2\pi} e^{i\left[k\phi\left(Y_1^*,\rho,\theta\right)-v\rho cos(\theta-\psi)-\frac{1}{2}u\rho^2\right]}\rho d\rho d\theta \quad (1)$$

in terms of basis functions, where u, v, and ψ are the optical coordinates.[15] This integral is defined such that the intensity is given by[15]

$$I(u,v,\psi) = |U(u,v,\psi)|^2. \quad (2)$$

For the diffraction pattern associated with a single aberration, Eq. (1) can be expanded in terms of Bessel functions J_n and Zernike Polynomials R_n^m[15]

$$U(u,v,\psi) = 4C\sum_{s=0}^{\infty'}(-i)^{(m-1)s}\cos(ms\psi) \times \int_0^1 e^{-\frac{1}{2}iu\rho^2}J_s\left[\alpha_{lnm}R_n^m(\rho)\right]J_{ms}(v\rho)\rho d\rho. \quad (3)$$

For small aberrations (i.e., where the constant α_{lnm} is small), the first Bessel function in the integral of Eq. (3) can be expanded in a power series; this lets us rewrite Eq. (3) as[15]

$$\begin{aligned}U(u,v,\psi) = C[&U_0(u,v,\psi) + i\alpha_{lnm}U_1(u,v,\psi)\\ &+ (i\alpha_{lnm})^2U_2(u,v,\psi)\\ &+ (i\alpha_{lnm})^3U_3(u,v,\psi)\\ &+ (i\alpha_{lnm})^4U_4(u,v,\psi) + ...],\end{aligned} \quad (4)$$

where the expansion terms are given by the integrals[15]

$$U_0 = 2\int_0^1 e^{-\frac{1}{2}iu\rho^2}J_0(v\rho)\rho d\rho, \quad (5)$$

$$U_1 = 2(-i)^m cos(m\psi) \times \int_0^1 e^{-\frac{1}{2}iu\rho^2}R_n^m(\rho)J_m(v\rho)\rho d\rho, \quad (6)$$

$$U_2 = \frac{1}{2!}\left\{\int_0^1 e^{-\frac{1}{2}iu\rho^2}\{R_n^m(\rho)\}^2J_0(v\rho)\rho d\rho + i^{2m}\cos(2m\psi)\int_0^1 e^{-\frac{1}{2}iu\rho^2}\{R_n^m(\rho)\}^2J_2m(v\rho)\rho d\rho\right\}, \quad (7)$$

$$U_3 = \frac{1}{2\times 3!}\{3(-i)^m\cos(m\psi) \times \int_0^1 e^{-\frac{1}{2}iu\rho^2}\{R_n^m(\rho)\}^3J_m(v\rho)\rho d\rho + i^{3m}\cos(3m\psi) \times \int_0^1 e^{-\frac{1}{2}iu\rho^2}\{R_n^m(\rho)\}^3J_{3m}(v\rho)\rho d\rho\}. \quad (8)$$

The constants l, n, and m are integers specifying the type of aberration, as shown in Table I.

TABLE I. Aberration types and integers (Ref. 15).

Aberration type	L	N	M
Spherical	0	4	0
Comatic	0	3	1
Astigmatic	0	2	2
Curvature	1	2	0
Distortion	1	1	1

B. Comatic aberration implementation

Recent experimental work[17] indicates that the presence of comatic aberration may enhance x-ray production via synchrotron radiation in a LWFA device. Therefore, the comatic aberration is the first aberration we study in detail. The expansion given by Eq. (4) was truncated after four terms; Eqs. (6)–(8) (the expression for U_4, while included in the calculations, is omitted below for brevity), yield

$$U_1 = i\cos(\psi)\frac{2J_4(v)}{v}, \quad (9)$$

$$U_2 = \frac{1}{2v}\left\{\frac{1}{4}J_1(v) - \frac{1}{20}J_3(v) + \frac{1}{4}J_5(v) - \frac{9}{20}J_7(v) - \cos(2\psi)\left[\frac{2}{5}J_3(v) + \frac{3}{5}J_7(v)\right]\right\}, \quad (10)$$

$$U_3 = \frac{-i}{12v}\left\{3\cos(m\psi)\left\{\frac{3}{14}J_{10}(v) - \frac{6}{35}J_8(v) + \frac{9}{70}J_6(v) - \frac{44}{105}J_4(v) + \frac{1}{15}J_2(v)\right\} + \cos(3m\psi)\left\{\frac{9}{28}J_{10}(v) + \frac{9}{20}J_6(v) - \frac{8}{35}J_4(v)\right\}\right\}. \quad (11)$$

Figure 1 shows the results of Eqs. (9)–(11), as well as the equation for U_4, for $\alpha \approx 1$, if the unperturbed pattern U_0 is take to be either an Airy pattern or a Gaussian pattern.

III. SIMULATION METHODOLOGY AND PARAMETERS

For this investigation, both two-dimensional and three-dimensional simulations were run using the particle-in-cell code OSIRIS 2.0. The three-dimensional version of the code was modified to explicitly include comatic aberrations. Both two- and three-dimensional simulations were performed; the

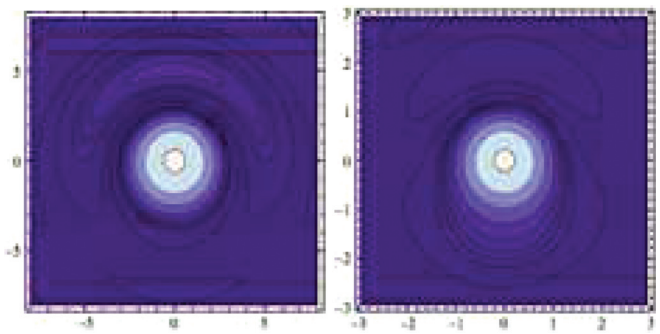

FIG. 1. (Color online) The intensities of an Airy pattern (left) and a Gaussian pattern (right) perturbed with an $\alpha = 1.005$ coma.

two-dimensional simulations permitted a thorough parameter sweep, while the three-dimensional simulations permitted an accurate depiction of the comatic aberration.

A. Two-dimensional simulations

For small perturbations in 2D, the superposition of TEM_{00} and TEM_{10} modes is similar to the coma aberration. Additionally, OSIRIS 2.0 can simulate this pulse structure without any modifications to the source code. For these reasons, preliminary simulations consisted of a TEM_{00} (i.e., a Gaussian) baseline pulse with a higher-order TEM_{10} pulse superimposed.

For the 2D simulations, the relative intensities of the pulses were varied to effect different degrees of mode mixing and asymmetry, while keeping the total pulse energy constant. Since pulse energy scales as the integral of a^2 over the volume of the pulse, pulse energy was kept constant by scaling the peak intensities of both the TEM_{00} and TEM_{10} pulses such that the following relationship was maintained for all simulations:

$$\int [\vec{a}_{00}(\vec{r}) + \vec{a}_{10}(\vec{r})]^2 dV = \int \vec{a}_0^2(\vec{r}) dV,$$

where $\vec{a}_0$ is a TEM_{00} pulse with peak intensity $a_0 = 4.0$. The relative intensities between the two pulses were quantified via the mixing fraction f_{10}

$$f_{00} \equiv \frac{a_{00}^2}{a_{00}^2 + a_{10}^2}, f_{10} \equiv \frac{a_{10}^2}{a_{00}^2 + a_{10}^2}.$$

Since the energy of the pulse is proportional to the integral of a^2, defining the mixing fraction in terms of a^2 is a natural choice. A computational sweep of this mixing fraction was performed; for brevity, these initial simulations were performed using the two-dimensional version of OSIRIS.

For all two-dimensional simulations, the maximum plasma density was $n_{max} = 0.01 n_{crit}$, or 1.75×10^{19} cm^{-3}. The simulation box size was $38.2 \times 63.7 \mu$m; the box moved at speed c in the laser propagation direction. The propagation time was 3475 fs, giving a propagation distance of 1.04 mm. The plasma density profile started with a linear ramp from $n = 0$ to $n = n_{max}$ over a distance of 63.5 μm, and ended with a linear ramp from $n = n_{max}$ to $n = 0$ over the same distance.

Computationally, the system was initialized with 2 particles per cell. The system had a grid size of 1200×500 (with the highest resolution in the propagation direction). This gave a grid spacing of $\Delta x \times \Delta y = 0.03185 \times 0.1274$ μm.

For the two-dimensional simulations, the laser pulse's full-width, half-maximum spot size was 5.1 μm. The pulse's full-width, half-duration was 35 fs. The normalized vector potentials of the two pulses were defined such that the total pulse energy was equivalent to that of a TEM_{00} pulse with a maximum normalized vector potential of $a_0 = 4.0$. This value of a_0 gives a peak pulse intensity of 3.5×10^{19}W/cm^2 for a pure TEM_{00} pulse.

The emittance, current, and energy characteristics of the electron beams produced were then measured. These parameters were determined by analyzing the final frame of the simulation, at which point the plasma density was zero, and the electron population could be assumed to consist entirely of the beam.

B. Three-dimensional simulations

The three-dimensional simulations consisted of a single Gaussian pulse, modified by a comatic aberration defined by the expansion parameter α. The parameter α was varied from 0.2 to 1.0 for the computational sweep. Since the parameter α, while mathematically convenient, is not directly measurable in experiment, Table II lists the Strehl ratios (i.e., the ratio of the peak Gaussian intensity to the peak aberrated intensity) equivalent to the simulated values of α.

For all three-dimensional simulations, the maximum plasma density was $n_{max} = 0.01 n_{crit}$, or 1.75×10^{19}cm^{-3}. The simulation box size was $38.1\ \mu\text{m} \times 31.8\ \mu\text{m} \times 31.8\ \mu$m; the box moved at speed c in the laser propagation direction. The propagation time was 3392 fs, yielding a propagation distance of 1.02 mm. As with the two-dimensional simulations, the plasma density profile started and ended with a linear ramp from $n = 0$ to $n = n_{max}$ over a distance of 63.5 μm.

Computationally, the system was initialized with 2 particles per cell. The system had a grid size of $1200 \times 250 \times 250$ (with the highest resolution in the propagation direction). This gave a grid spacing of $\Delta x \times \Delta y \times \Delta z = 0.03175 \times 0.1272 \times 0.1272$ μm.

As with the two-dimensional simulations, the laser pulse's full-width, half-maximum spot size was 5.1 μm and the pulse's full-width, half-duration was 35 fs. Again, as with the two-dimensional simulations, the emittance, current, and energy characteristics of the electron beams produced were then measured by analyzing the final frame of the simulation.

For the expansion shown in Eq. (3), the pulse power, proportional to the integral

$$P \propto \int a^2(\vec{r}) dx dy$$

remains constant as α is varied. If the expansion given by Eq. (4) is truncated after four terms, the total pulse power varies by an average of 0.76%, no more than 2.19%, over the range $0 \leq \alpha \leq 1$. Therefore, by utilizing the same pulse initialization parameters, the pulse energy in the 3D simulations was kept approximately constant as α was varied. For the unaberrated pulse, these parameters yielded a peak

TABLE II. Strehl coefficients for the given alpha values.

Parameter α	Strehl ratio
0.0	0.0
0.2	0.995
0.4	0.980
0.6	0.956
0.8	0.923
1.0	0.882

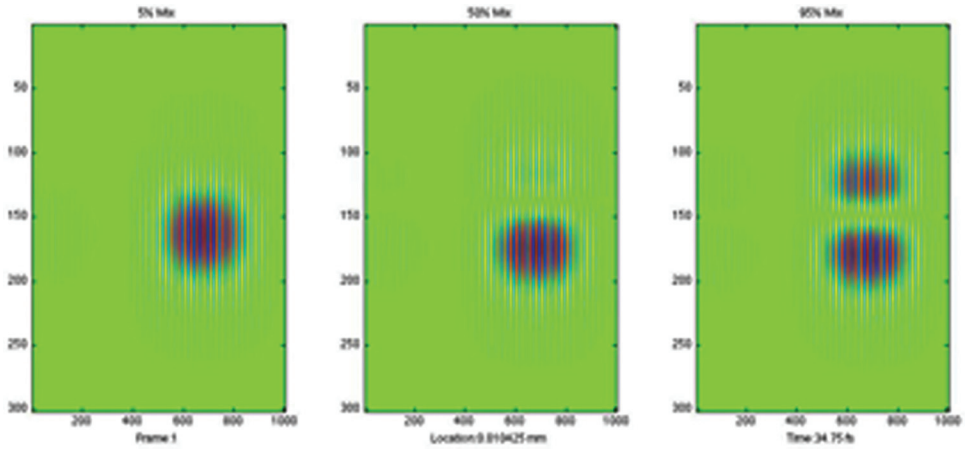

FIG. 2. (Color online) The initial laser pulses for mixing fractions of, from left to right, 5%, 50%, and 95%.

normalized vector potential of $a_0 = 4.0$ and a peak intensity of $3.5 \times 10^{19}\mathrm{W/cm}^2$.

C. Parameter characterization

For the three-dimensional simulations, the current data was extracted directly from the code. The peak forward current, i.e., the current parallel to the direction of laser propagation, was calculated from these distributions.

The beam emittance was calculated from

$$\varepsilon_i = 4\langle \Delta x_i \rangle \langle \Delta v_i \rangle,$$

where the subscript i denotes whether or not the positions, and velocities are taken in the polarization direction or perpendicular to the polarization direction. The quantity $\langle \Delta x_i \rangle$ is the root-mean-square deviation of the particle position from the mean particle position in the i^{th} direction, and the quantity $\langle \Delta v_i \rangle$ is the root-mean-square deviation of the particle velocity from the mean particle velocity in the i^{th} direction, as a fraction of the velocity in the propagation direction.

Since OSIRIS prints the relativistic factor γ, calculating the beam energy distribution from the printed gamma distribution via $E = (\gamma - 1)m_0c^2$ was straightforward. For the three-dimensional simulations, the peak beam energies were calculated from the maximum of the energy spectra. However, for the two-dimensional simulations, the average beam energies were taken, as the two-dimensional energy spectra did not have clearly defined single energy peaks.

IV. 2D TEM_{00} / TEM_{10} MODE-MIXING PRELIMINARY SIMULATION RESULTS

Figure 2 shows, respectively, the initial laser pulse for the two-dimensional, mode-mixing simulations at mixing fractions of 0.05, 0.50, and 0.95. The results of these simulations are shown in Figs. 3 and 4.

Figure 3 shows the relationship between the beam's perpendicular emittance and the mode mixing fraction. The TEM 10 mode is functionally similar to a pair of copropagating pulses with 180 degree phase shift; it has been shown[16] that the nonlinear interaction of two such pulses will cause them to repel, resulting in the observed increase in the final beam emittance.

Figure 4 shows the relationship between the beam's peak energy and the mode mixing fraction. The beam energy showed a fairly strong negative correlation with the mixing fraction ($R^2 \approx 0.75$), decreasing by roughly a factor of 2, from $\sim$140 to $\sim$70MeV, over the course of the parameter sweep.

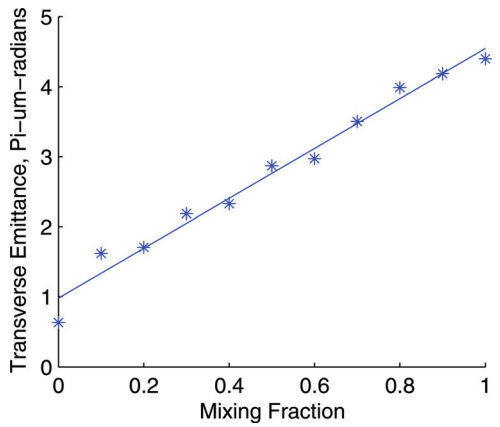

FIG. 3. (Color online) The effect of mode mixing on the 2D perpendicular beam emittance.

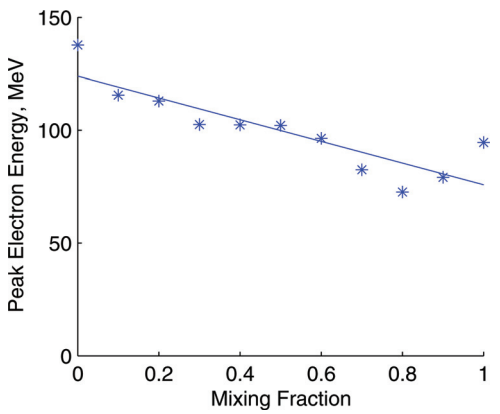

FIG. 4. (Color online) The effect of mode mixing on the 2D beam averaged energy.

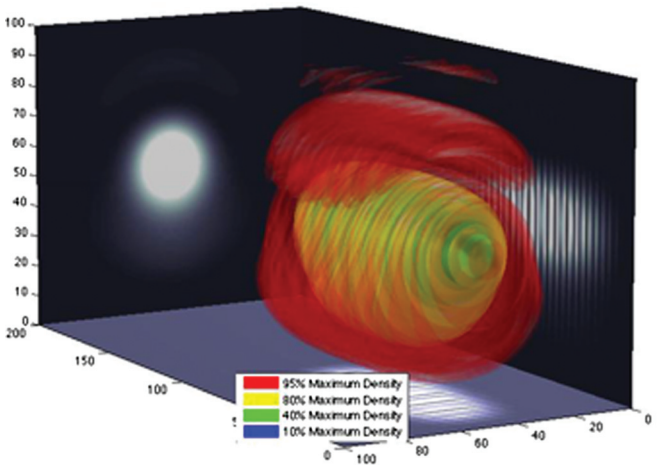

FIG. 5. (Color online) The 3D intensity profile of the pulse for an aberration coefficient $\alpha = 1.005$.

V. 3D EXPLICIT COMA SIMULATION RESULTS

Figure 5 shows the intensity profile for a three-dimensional simulation with an $\alpha = 1.005$ coma. The results of the three-dimensional simulations including a direct calculation of the comatic aberration are shown in Figs. 6–9.

Figure 6 shows the relationship between the aberration coefficient α and the peak beam current. The current varies by 20% over the parameter range, with a correlation of $R^2 = 0.74$. This does not appear to have a dramatic impact on the beam performance, as even after a severe aberration is applied, the peak current varies by less than 20%.

Figure 7 shows the relationship between the aberration coefficient α and the peak beam energy. The peak energies vary by less than 10% over the entire parameter range, with a correlation of only $R^2 = 0.58$. These results indicate that even in the presence of a severe aberration, peak beam energy is relatively unaffected.

Figure 8 shows how the shape of the beam electron energy spectra varies with α. This figure shows that there is a weak relationship between the beam energy spread or general shape of the energy spectrum and the aberration strength.

Figure 9 shows the relationship between the aberration coefficient α and both the polarization (top) and perpendicular (bottom) emittances. Note that the primary aberration axis was in the polarization direction; Fig. 9 shows that a strong comatic aberration increases polarization emittance noticeably, while leaving the perpendicular emittance relatively unaltered.

The difference between the polarization and perpendicular emittances indicates that there is a high degree of beam ellipticity. This condition enhances x-ray generation by synchrotron radiation[14] and indicates that off-axis electron injection may be occurring. This off-axis injection would increase the amplitude of the betatron oscillations[13,14] in the

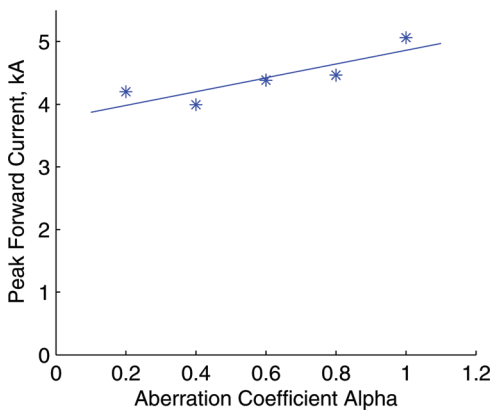

FIG. 6. (Color online) The effect of a comatic aberration on the 3D peak beam current.

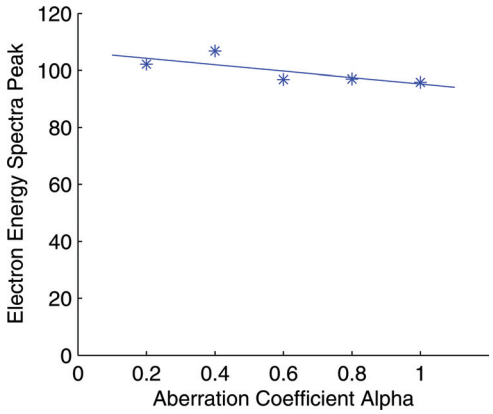

FIG. 7. (Color online) The effect of a comatic aberration on the 3D peak beam energies.

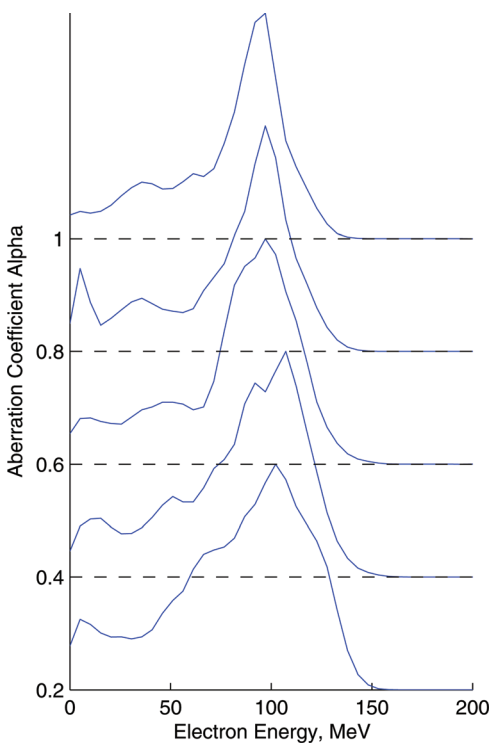

FIG. 8. (Color online) The effect of a comatic aberration on the 3D beam electron energy spectra; note that the spectral heights have been arbitrarily scaled for clarity; the corresponding values of α are, from bottom to top: $\alpha = 0.2, 0.4, 0.6, 0.8,$ and 1.0.

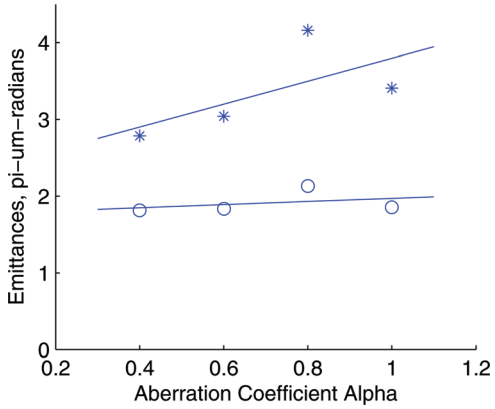

FIG. 9. (Color online) The effect of a comatic aberration on both the polarization (top) and perpendicular (bottom) 3D beam emittances.

undulating electron beam. Therefore, these results support the conclusions of recent experimental work indicating that a comatic aberration can increase the amplitude of the betatron oscillations in a laser-wakefield accelerator.[14] Confirmation of these effects would require a more focused computational investigation, including considering the case where the primary aberration axis and polarization axis are perpendicular.

VI. CONCLUSION

The results of this computational sweep are promising on two fronts. First, the results indicate that the performance of a LWFA device will be relatively unaffected by the presence of even a strong comatic aberration. Neither the peak beam energy nor the electron energy spread were significantly affected by the presence of a strong comatic aberration for the three-dimensional simulations. Second, the trends in perpendicular and polarization emittances indicate that the beam ellipticity increases with the strength of the comatic aberration. This supports recent experimental work indicating that the presence of a coma can enhance the production of x-rays via synchrotron radiation.

ACKNOWLEDGMENTS

This work was supported by the NSF/DOE under grant (PHY-09-03557). The authors would like to acknowledge the OSIRIS Consortium (UCLA, IST Portugal) for the use of the OSIRIS 2.0 framework. The authors would also like to acknowledge the support of the Michigan Institute for Plasma Science and Engineering.

[1]T. Tajima and J. M. Dawson, Phys. Rev. Lett. **43**, 267 (1979).
[2]C. B. Schroeder, E. Esarey, C. G. R. Geddes, C. Benedetti, and W. P. Leemans, Phys. Rev. ST Accel. Beams **13**, 101301 (2010).
[3]M. Sadeghi, M. Enferadi, and A. Shirazi, J. Cancer Res. Ther. **6**, 239 (2010).
[4]W. Ludwig, A. King, M. Herbig, P. Reischig, J. Marrow, L. Babout, E. M. Lauridsen, H. Proudhon, and J. Y. Buffiere, JOM **62**(12), 22 (2010).
[5]A. Sakdinawat and D. Attwood, Nature Photon. **4**(12), 840 (2010).
[6]D. P. Pritzkau and R. H. Siemann, Phys. Rev. ST Accel. Beams **5**, 112002 (2002).
[7]E.-S. Kim and M. Yoon, IEEE Trans. Nucl. Sci. **56**, 3597 (2009).
[8]E. Brunetti, R. P. Shanks, G. G. Manahan, M. R. Islam, B. Ersfeld, M. P. Anania, S. Cipiccia, R. C. Issac, G. Raj, G. Vieux, G. H. Welsh, S. M. Wiggins, and D. A. Jaroszynski, Phys. Rev. Lett. **105**, 215007 (2010).
[9]S. Kneip, C. McGuffey, J. L. Martins, S. F. Martins, C. Bellei, V. Chvykov, F. Dollar, R. Fonseca, C. Huntington, G. Kalintchenko *et al.*, Nat. Phys. **6**(12), 980 (2010).
[10]C. M. S. Sears, A. Buck, K. Schmid, J. Mikhailova, F. Krausz, and L. Veisz, Phys. Rev. ST Accel. Beams **13**, 092803 (2010).
[11]M. C. Kaluza, S. P. D. Mangles, A. G. R. Thomas, Z. Najmudin, A. E. Dangor, C. D. Murphy, J. L. Collier, E. J. Divall, P. S. Foster, C. J. Hooker, A. J. Langley, J. Smith, and K. Krushelnik, Phys. Rev. Lett. **105**, 095003 (2010).
[12]A. Popp, J. Vieira, J. Osterhoff, Zs. Major, R. Horlein, M. Fuchs, R. Weingartner, T. P. Rowlands-Rees, M. Marti, R. A. Fonseca, S. F. Martins, L. O. Silva, S. M. Hooker, F. Krausz, F. Gruner, and S. Karsch, Phys. Rev. Lett. **105**, 215001 (2010).
[13]Y. Glinec, J. Faure, A. Lifschitz, J. M. Vieira, R. A. Fonseca, L. O. Silva, and V. Malka, EPL **81**, 64001 (2008).
[14]S. P. D. Mangles, G. Genoud, S. Kneip, M. Burza, K. Cassou, B. Cros, N. P. Dover, C. Kamperidis, Z. Najmudin, A. Persson *et al.*, Appl. Phys. Lett. **95**, 181106 (2009).
[15]M. Born and E. Wolf, *Principles of Optics* (Pergamon, New York 1975).
[16]C. Ren, B. Duda, R. Evans, R. Fonseca, R. Hemker, and W. Mori, Phys. Plasmas **9**, 2354 (2002).
[17]K. T. Phuoc, S. Corde, R. Fitour, R. Shah, F. Albert, J.-P. Rousseau, F. Burgy, A. Rousse, V. Seredov, and A. Pukhov, Phys. Plasmas **15**, 073106 (2008).